Computers and Fluids 244 (2022) 105545

Contents lists available at ScienceDirect

Computers and Fluids

journal homepage: www.elsevier.com/locate/compfluid

High-order discontinuous Galerkin approximation for a three-phase incompressible Navier–Stokes/Cahn–Hilliard model

Juan Manzanero [a,b,*], Carlos Redondo [a,b], Miguel Chávez-Módena [a,b], Gonzalo Rubio [a,b], Eusebio Valero [a,b], Susana Gómez-Álvarez [c], Ángel Rivero-Jiménez [c]

[a] ETSIAE-UPM - School of Aeronautics, Universidad Politécnica de Madrid, Plaza Cardenal Cisneros 3, E-28040 Madrid, Spain
[b] Center for Computational Simulation, Universidad Politécnica de Madrid, Campus de Montegancedo, Boadilla del Monte, 28660, Madrid, Spain
[c] Repsol Technology Lab Agustín de Betancourt S/N, 28935, Móstoles, Madrid, Spain

ARTICLE INFO

Keywords:
Navier–Stokes
Cahn–Hilliard
Computational fluid dynamics
High-order methods
Discontinuous Galerkin
Three-phase flows
Oil and gas transport

ABSTRACT

In this work we introduce the development of a three-phase incompressible Navier–Stokes/Cahn–Hilliard numerical method to simulate three-phase flows, present in many industrial operations. The numerical method is then applied to successfully solve oil transport problems, such as those found in the oil and gas industry. The three-phase model adopted in this work is a Cahn–Hilliard diffuse interface model, which was derived by Boyer and Lapuerta (2006). The Cahn–Hilliard model is coupled to the kinetic-energy stable incompressible Navier–Stokes equations model derived by Manzanero et al. (2020). The spatial discretization uses a high-order discontinuous Galerkin spectral element method which yields highly accurate results in arbitrary geometries. An implicit–explicit (IMEX) method is adopted as temporal scheme for the Cahn–Hilliard equation, while Runge–Kutta 3 (RK3) is used for the Navier–Stokes equations. The developed numerical tool is validated with a manufactured solution test case and used to simulate multiphase flows in pipes, including and a three-phase T-shaped pipe intersection.

1. Introduction

The transportation of hydrocarbons from the reservoir to the processing facilities is characterized by the modification on flowing pressure and temperature conditions. These changes in operational conditions lead to a transition from typical one-phase behavior to a more complex multiphase flow with different number of phases present along the production system (wells, flowlines, export lines, ...). The vast majority of the reservoirs present fluids which evolve into a mixture of liquid crude oil, natural gas and water. In case flowing bottom whole pressures at the near well location are below certain values, even sand particles or fines can be dragged and produced with the stream, leading to a more complex flow.

The physical phenomena associated with hydrocarbon multiphase flow transport (e.g., change in the flow pattern or phase change) will impact the production process or even lead to safety issues (e.g., liquid overflooding in process facilities due to an underestimation of liquid surges caused by slug flow). Therefore, an accurate prediction of the flow distribution and behavior is mandatory to ensure reliable and continuous transport of the production fluid. In the last years, numerical techniques for simulating multiphase flows have reached a high level of maturity, which have led to their widespread use in many industries, such as energy, automotive or aerospace. This is due both to the improvements in multiphase flow models and the increase in computational power with HPC facilities (which, at the same time, limits its application in daily or routine engineering analysis). The petroleum industry can take advantage from high fidelity multiphase flow simulation tools to minimize the cost of production system design as well as to support the optimization of its operation.

In the oil and gas industry, multiphase flows are usually modeled with one-dimensional (1D) simulations tools (e.g. OLGA®, Pipesim® or LedaFlow®[1]). These models rest on a large number of experimental databases, which results in accurate results with a low computational cost [1]. However these 1D modeling tools are limited as they cannot capture some physical details, specially where three-dimensional effects are important. This means that resolving fast transient phenomena (e.g., slug flow) still presents limitations in current 1D modeling tools [2]. A different approach is followed by multiphase flow simulation based on Computational Fluid Dynamics (CFD), that permits detailed three-dimensional (3D) simulations of immiscible fluids including effects of pressure, temperature and liquid–gas heat and mass

* Corresponding author at: ETSIAE-UPM - School of Aeronautics, Universidad Politécnica de Madrid, Plaza Cardenal Cisneros 3, E-28040 Madrid, Spain.
E-mail address: juan.manzanero@upm.es (J. Manzanero).

[1] OLGA® / Pipesim® are registered trademarks of Schlumberger Inc. and LedaFlow® is a registered trademark of Kongsberg A/S.

https://doi.org/10.1016/j.compfluid.2022.105545
Received 30 May 2021; Received in revised form 24 April 2022; Accepted 8 June 2022
Available online 14 June 2022

transfer. The main objectives of these simulations is to provide detailed qualitative and quantitative evaluation of flow assurance issues, such as erosion or slugging, supporting designers and operators to solve flow problems or to extend the life of the flow lines.

Interface capturing methods are among the simplest approaches to treat multiphase flows in CFD. In these models, the governing equations are the continuity and momentum equations for a divergence-free velocity field, in conjunction with a convective equation that tracks the interface. Among interface capturing methods, such as Volume of Fluid (VOF) [3] or Level Set [4]; Diffuse Interface (DI) methods (also known as phase field methods) [5–7] provide a useful alternative that does not seem to suffer from problems with either mass conservation or the accurate computation of surface tension. Although there are examples of three phase flows (or in general, N-phase flows, with N greater or equal than 3) with Level Set or VOF methods [8–16], most of the work in three phase flows is based on DI methods [17–28]. In this paper we focus in the phase field approach.

In DI methods, a phase-field function that describes the N-phase system is defined. The sharp fluid interface is replaced by a smooth transition layer that connects the two immiscible fluids. The free-energy, which represents the effect of the surface tension between the different fluids, is used to characterize the system. The free-energy presents two terms whose effect tend to mix the fluids and separate the fluids respectively [29,30]. The evolution of the phase-field function in our work is modeled by means of the convective Cahn–Hilliard (CH) equation [31]. The use of the CH equation for the evolution of the phase-field function permits an accurate computation of the surface tension and the simulation of phase separation processes. In particular, in this work we use the model of Boyer et al. [17] to describe the three-phase system coupled to the incompressible Navier–Stokes (iNS) equations with variable density and artificial (or *pseudo*) compressibility [32]. A review of alternative iNS/CH models can be found in [33].

The three-phase model is numerically approximated in space with a high-order Discontinuous Galerkin Spectral Element Method (DGSEM) [34] that uses the Symmetric Interior Penalty (SIP) method [35–39]. The DGSEM has been used in the past to discretize multiphase (two phase) flows [40–44], and it is popular for its arbitrary order of accuracy [34,45], low dissipative and dispersive errors [46–49], the representation of arbitrary three-dimensional complex geometries through the use of unstructured meshes with curvilinear elements [50], efficient mesh adaptation techniques [51–53] and the design of provably stable schemes [43,54–59]. Previously, three component Cahn–Hilliard models have been discretized by means of the finite element method [19], local discontinuous Galerkin method [60] or spectral element method [61]. The DGSEM has been used in the past to discretize the two component Cahn–Hilliard equation [58] and the three component Cahn–Hilliard equation [62]. To the authors' knowledge, this is the first implementation of the three component Cahn–Hilliard model [63] coupled with the Navier–Stokes equations in a discontinuous Galerkin framework.

Finally, for the discretization of time of the Cahn–Hilliard equation we consider a first-order IMplicit–EXplicit (IMEX) time integrator. The linear fourth order spatial operator of the Cahn–Hilliard equation is solved implicitly while the non-linear second order spatial operator is treated explicitly. The solution of the fully-discrete system involves the solution of one linear system for each of the Cahn–Hilliard equations (two for the three phase system). As detailed in [62], the two linear systems are decoupled such that the Jacobian matrices are constant in time and identical for both Cahn–Hilliard equations. Therefore this method permits a resolution in which only one LU factorization is performed for the two equations. The Navier–Stokes equations are solved by means of a third order low-storage explicit Runge–Kutta RK3 method [64]. Therefore the low-order temporal approximation is used exclusively to approximate the diffusive contribution of the Cahn–Hilliard equation. The diffusive contribution of the Cahn–Hilliard equation is an artifact tailored by its authors to engineer diffuse interfaces and phase separation, and it is not directly connected to the macroscopic physical characteristics of interest of the flow, such as the density or the viscosity. Therefore, the use of a lower order scheme is not incompatible with the use of a high-order scheme in the Navier–Stokes equations. In the Navier–Stokes equations, however, the use of a high-order method has the advantage of a lower numerical dissipation, which prevents turbulent flow structures to quickly diffuse back into the flow. It is important to note that the interfaces produced by the Cahn–Hilliard will not be numerically diffused by the lower-order approximation, since the chemical free energy controls the sharpening back the interface.

The numerical method presented in this work has been successfully used to compute the flow to predict erosion and corrosion in oil and gas pipes [65].

The rest of this work is organized as follows: we write the governing equations in Section 2, and we construct its DG approximation and the IMEX time discretization in Section 3. Finally, we present numerical experiments for the two-phase and three-phase version of the model in Section 4.

2. Governing equations

In this work, we couple the three-phase Cahn–Hilliard model of Boyer et al. [17,62] to the incompressible Navier–Stokes equations with artificial compressibility [59]. We define the concentration of phase j as the relative volume occupied by that phase. Thus, for three-phase flows we have that

$$c_1 + c_2 + c_3 = 1. \tag{1}$$

Henceforth, without loss of generality, we consider that the concentrations of phases 1 and 2 can freely vary, and we compute the concentration of phase 3 from (1). For phases 1 and 2, the concentration is computed from the Cahn–Hilliard equation,

$$c_{i,t} + \vec{\nabla}\cdot\left(c_i\vec{u}\right) = \frac{M_0}{\Sigma_i}\vec{\nabla}\cdot\left(\vec{\nabla}\mu_i\right), \quad i = 1,2, \tag{2}$$

where $\vec{u} = (u, v, w)$ is the velocity field, M_0, is the mobility and μ_i is the chemical potential of phase i,

$$\mu_i = \frac{12}{\epsilon}\Sigma_i f_i - \frac{3}{4}\epsilon\Sigma_i\vec{\nabla}^2 c_i, \quad i = 1,2,3, \tag{3}$$

with

$$f_i = \frac{\Sigma_T}{3\Sigma_i}\sum_{\substack{j=1\\ j\neq i}}^{3}\left(\frac{1}{\Sigma_j}\left[\frac{\partial F_0^\sigma}{\partial c_i} - \frac{\partial F_0^\sigma}{\partial c_j}\right]\right), \quad \frac{3}{\Sigma_T} = \frac{1}{\Sigma_1} + \frac{1}{\Sigma_2} + \frac{1}{\Sigma_3}. \tag{4}$$

The chemical potentials are algebraically constrained [17],

$$\frac{\mu_1}{\Sigma_1} + \frac{\mu_2}{\Sigma_2} + \frac{\mu_3}{\Sigma_3} = 0, \tag{5}$$

where Σ_i and ϵ are positive constants called *spreading factors* and interface width, respectively. The *spreading factors* are computed from the interfacial tension between the two phases,

$$\Sigma_i = \sigma_{ij} + \sigma_{ik} - \sigma_{jk}, \quad (i,j,k) \text{ cyclical}. \tag{6}$$

Finally, as in [17], the *chemical free-energy* F_0^σ is a polynomial function on the concentrations,

$$F_0^\sigma = \sigma_{12}c_1^2c_2^2 + \sigma_{13}c_1^2c_3^2 + \sigma_{23}c_2^2c_3^2 + c_1c_2c_3\left(\Sigma_1c_1 + \Sigma_2c_2 + \Sigma_3c_3\right). \tag{7}$$

The density (and all the thermodynamic variables) is computed from the concentration of the three phases,

$$\rho\left(c_1,c_2,c_3\right) = \rho_1c_1 + \rho_2c_2 + \rho_3c_3 = \rho_1c_1 + \rho_2c_2 + \rho_3\left(1 - c_1 - c_2\right), \tag{8}$$

where $\rho_{1,2,3}$ are the densities of fluids 1, 2 and 3, respectively, assumed constant in space and time. The velocity field is given by the momentum equation,

$$\left(\rho\vec{u}\right)_t + \vec{\nabla}\cdot\left(\rho\vec{u}\vec{u}\right) = -\vec{\nabla}p + \sum_{m=1}^{3}\mu_m\vec{\nabla}c_m + \vec{\nabla}\cdot\left(\eta\left(\vec{\nabla}\vec{u} + \vec{\nabla}\vec{u}^T\right)\right) + \rho\vec{g}, \tag{9}$$

where η is the viscosity, computed from the (constant) equilibrium phases viscosities $\eta_{1,2,3}$ in a similar fashion to the density (see Eq. (8)). The sum of the $\mu_m \nabla c_m$ products is the phase field approximation of the capillary pressure, and $\vec{g}$ is the gravity acceleration.

The pressure is computed with an artificial compressibility model [66,67],

$$p_t + \rho_0 c_0^2 \vec{\nabla} \cdot \vec{u} = 0, \tag{10}$$

with $\rho_0 = \max(\rho_1, \rho_2, \rho_3)$ and c_0 the artificial compressibility sound speed. The artificial compressibility model substitutes the divergence-free condition of incompressible flows by a hyperbolic equation. By design, it converges to the incompressible flow solution when a steady-state is reached, whereas it provides a suitable approximation in transient simulations. The artificial sound speed value is chosen following a compromise between accuracy (higher values) and stiffness/time-step restriction (lower values). Throughout this work, as recommended in [59] we adopt the value $c_0^2 = 10^3$.

The governing equations (2), (9) and (10) are written as a general advection–diffusion equation,

$$\mathbf{q}_t + \nabla \cdot \vec{\mathbf{f}}_e(\mathbf{q}) = \nabla \cdot \vec{\mathbf{f}}_v(\mathbf{q}, \nabla \mathbf{w}) + \mathbf{s}(\mathbf{q}, \nabla \mathbf{w}), \tag{11}$$

with the state vector $\mathbf{q} = (c_1, c_2, \rho\vec{u}, p)$, gradient variables $\mathbf{w} = (\mu_1/\Sigma_1, \mu_2/\Sigma_2, \rho\vec{u}, p)$, inviscid and viscous fluxes,

$$\mathbf{f}_e = \begin{pmatrix} c_1 u & c_1 v & c_1 w \\ c_2 u & c_2 v & c_2 w \\ \rho u^2 + p & \rho uv & \rho uw \\ \rho uv & \rho v^2 + p & \rho vw \\ \rho uw & \rho vw & \rho w^2 + p \\ \rho_0 c_0^2 u & \rho_0 c_0^2 v & \rho_0 c_0^2 w \end{pmatrix}, \quad \mathbf{f}_v = \begin{pmatrix} \frac{M_0}{\Sigma_1}\mu_{1,x} & \frac{M_0}{\Sigma_1}\mu_{1,y} & \frac{M_0}{\Sigma_1}\mu_{1,z} \\ \frac{M_0}{\Sigma_2}\mu_{2,x} & \frac{M_0}{\Sigma_2}\mu_{2,y} & \frac{M_0}{\Sigma_2}\mu_{2,z} \\ 2\eta \mathrm{s}_{11} & 2\eta \mathrm{s}_{12} & 2\eta \mathrm{s}_{13} \\ 2\eta \mathrm{s}_{21} & 2\eta \mathrm{s}_{22} & 2\eta \mathrm{s}_{23} \\ 2\eta \mathrm{s}_{31} & 2\eta \mathrm{s}_{32} & 2\eta \mathrm{s}_{33} \\ 0 & 0 & 0 \end{pmatrix} \tag{12}$$

and source term,

$$\mathbf{s}(\mathbf{q}, \nabla \mathbf{w}) = \begin{pmatrix} 0 \\ 0 \\ \rho g_1 + \mu_1 c_{1,x} + \mu_2 c_{2,x} + \mu_3 c_{3,x} \\ \rho g_2 + \mu_1 c_{1,y} + \mu_2 c_{2,y} + \mu_3 c_{3,y} \\ \rho g_3 + \mu_1 c_{1,z} + \mu_2 c_{2,z} + \mu_3 c_{3,z} \\ 0 \end{pmatrix}. \tag{13}$$

In Eq. (12), $\mathrm{s} = \frac{1}{2}(\nabla \vec{u} + \nabla \vec{u}^T)$ is the strain tensor.

2.1. Reduction of the model to a two-phase flow model

Constructed this way, the chemical potential satisfies an important consistency property: when one phase is not initially present (e.g. phase 2), the chemical potential associated to that phase is zero [17],

$$\mu_2\Big|_{c_2=0} = 0, \tag{14}$$

and the chemical potential associated to the other two phases, which satisfy $c_1 + c_3 = 1$, reduces to that of a two-phase model [17,62]. We compute the chemical free-energy derivatives for $c_2 = 0$, $c_1 = c$, and $c_3 = 1 - c$,

$$\begin{aligned} \frac{\partial F_0^\sigma}{\partial c_1} &= 2\sigma_{13} c_1 c_3^2 = (\Sigma_1 + \Sigma_3) c_1 c_3^2 = (\Sigma_1 + \Sigma_3) c (1-c)^2, \\ \frac{\partial F_0^\sigma}{\partial c_2} &= c_1 c_3 (\Sigma_1 c_1 + \Sigma_3 c_3) = c(1-c)(\Sigma_1 c + \Sigma_3 (1-c)), \\ \frac{\partial F_0^\sigma}{\partial c_3} &= 2\sigma_{13} c_1^2 c_3 = (\Sigma_1 + \Sigma_3) c_1^2 c_3 = (\Sigma_1 + \Sigma_3) c^2 (1-c), \end{aligned} \tag{15}$$

which are replaced into the chemical potential (see Eq. (3)), defining $c = c_j$ and $c_k = 1 - c$,

$$\begin{aligned} \mu_1\Big|_{\substack{c_1=c \\ c_2=0 \\ c_3=1-c}} &= \frac{12\Sigma_1}{\varepsilon}\left(c(1-c)^2 - c^2(1-c)\right) - \frac{3}{4}\Sigma_1 \varepsilon \nabla^2 c, \\ &= \frac{\Sigma_1}{2\sigma_{13}}\left(\frac{12\sigma_{13}}{\varepsilon}\frac{\mathrm{d}}{\mathrm{d}c}\left(c^2(1-c^2)\right) - \frac{3}{2}\sigma_{13}\varepsilon\nabla^2 c\right) = \frac{\Sigma_1}{2\sigma_{13}}\mu^{2\mathrm{ph}}. \end{aligned} \tag{16}$$

The three-phase flow model also reduces to a two-phase model if one of the concentrations is not present initially. If phase 2 is not initially present, $c_2(\vec{x}, 0) = 0$, the second Cahn–Hilliard equation is

$$c_{2,t} = -\vec{\nabla} \cdot (c_2 \vec{u}) + \frac{M_0}{\Sigma_2}\vec{\nabla}^2 \mu_2 = 0, \tag{17}$$

since $\mu_2 = 0$ when $c_2 = 0$, as described in Eq. (14). Therefore, $c_2(\vec{x}, t) = 0$ for $t > 0$, and phase 2 will not show in later times. Whereas for phase 1, its Cahn–Hilliard equation is simplified to

$$c_t + \nabla \cdot (c\vec{u}) = \frac{M_0}{2\sigma_{13}}\nabla^2 \mu^{2\mathrm{ph}}, \tag{18}$$

which corresponds to a two-phase Cahn–Hilliard model with an adjusted mobility, $\frac{M_0}{2\sigma_{13}}$.

Lastly, we check that the capillary pressure term of the three-phase flow also reduces to that of a two-phase flow. For three phases,

$$\begin{aligned} \vec{p}_c &= \mu_1 \vec{\nabla} c_1 + \mu_2 \vec{\nabla} c_2 + \mu_3 \vec{\nabla} c_3 = \mu_1 \vec{\nabla} c_1 + \frac{\Sigma_3}{\Sigma_1}\mu_1 \vec{\nabla} c_1 \\ &= \frac{\Sigma_1 + \Sigma_3}{\Sigma_1}\mu_1 \vec{\nabla} c_1 = \frac{2\sigma_{13}}{\Sigma_1}\mu_1 \vec{\nabla} c_1 = \mu^{2ph} \vec{\nabla} c. \end{aligned} \tag{19}$$

Therefore, we confirm that the approximation for the capillary pressure is identical in both models. In the second line, we used the property $\Sigma_i + \Sigma_j = 2\sigma_{ij}$ of the spreading factors, $\nabla c_3 = -\nabla c_1$, and $\mu_3/\Sigma_3 = -\mu_1/\Sigma_1$ (see Eqs. (1), (5) and (6)).

We conclude that the three-phase model is a valid two-phase model if one of the three phases is not present initially.

3. Discontinuous Galerkin method and IMEX scheme

The evolution of the three-phase flow is driven by the two Cahn–Hilliard equations (see Eq. (2)), the momentum Eq. (9), and the artificial compressibility Eq. (10). The discretization of the spatial differential operators is performed using a nodal Discontinuous Galerkin Spectral Element Method (DGSEM), described in Section 3.1, and the discretization of the time derivatives is performed using an IMplicit–EXplicit (IMEX) method, detailed in Section 3.2. The latter combines a third order low-storage explicit Runge–Kutta RK3 method [64], and a first-order backward and forward Euler method.

3.1. Spatial discretization using the DGSEM

The system of Eqs. (11) is approximated in space with a high-order discontinuous Galerkin method. The computational domain Ω is tessellated in non-overlapping hexahedral elements e. Both the solution and the geometry are approximated by order N polynomials, and thus the elements can be curvilinear. We establish a transfinite mapping as in [50,58] that transforms the unit cube $E = [-1, 1]^3$ (known as the *reference element*) to an arbitrarily-shaped hexahedral element e (see Fig. 1). Thus, we work on the reference space (ξ, η, ζ) where the reference element E is defined, and then its coordinates are related to the physical space with the mapping $(x, y, z) = \vec{X}(\xi, \eta, \zeta)$.

We define a set of tensor product Gauss–Lobatto (GL) points $(\xi_i, \eta_j, \zeta_k)_{i,j,k=0}^N$ [34], which we use to approximate the solution by order N polynomials,

$$\mathbf{q}\Big|_e \approx \mathrm{I}^N(\mathbf{q}) = \mathbf{Q} = \sum_{i,j,k=0}^{N} \mathbf{Q}_{ijk}(t) l_i(\xi_i) l_j(\eta_j) l_k(\zeta_k), \tag{20}$$

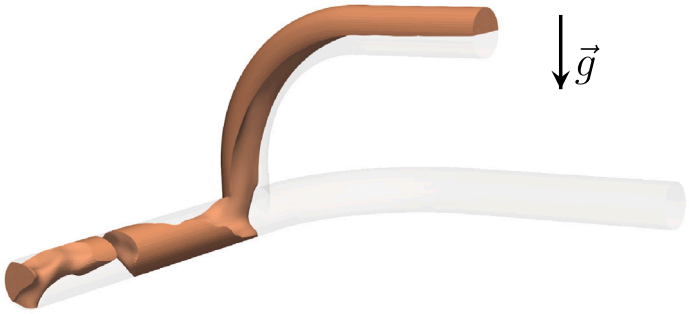

Fig. 1. Elements geometrical transformation from the reference element $E = [-1,1]^3$ to their final shape and position on the physical space. The transformation uses a transfinite order N mapping $\vec{x}\left(\vec{\xi}\right)$. The tensor product Gauss–Lobatto points are also transformed.

where $\mathbf{Q}_{ijk}$ are the nodal coefficients, and l_i are the Lagrange interpolating polynomials. The GL points also define quadrature rules that approximate the integrals on the reference element,

$$\langle f,g\rangle_E \approx \langle F,G\rangle_{E,N} = \sum_{i,j,k=0}^{N} w_{ijk}F_{ijk}G_{ijk}, \tag{21}$$

where $w_{ijk} = w_i w_j w_k$ are the tensor product quadrature weights [34].

We define the covariant and contravariant basis to relate the derivatives in the reference (∇_ξ) and physical (∇) spaces,

$$\vec{a}_i = \frac{\partial \vec{X}}{\partial \xi^i}, \quad \vec{a}^i = \nabla\xi^i = \frac{\vec{a}^j \times \vec{a}^k}{J}, \quad J = \vec{a}_1 \cdot \left(\vec{a}_2 \times \vec{a}_3\right), \quad (i,j,k) \text{ cyclic}, \tag{22}$$

which allow us to compute the gradient of a scalar and the divergence of a vector as,

$$J\nabla \mathbf{w}_i = \mathcal{M}\nabla_\xi \mathbf{w}_i, \quad J\nabla\cdot\vec{\mathbf{f}}_i = \nabla_\xi\cdot\vec{\tilde{\mathbf{f}}}_i, \quad \vec{\tilde{\mathbf{f}}}_i = \mathcal{M}^T\vec{\mathbf{f}}_i, \quad \mathcal{M} = \left(J\vec{a}^\xi, J\vec{a}^\eta, J\vec{a}^\zeta\right). \tag{23}$$

Discretely, the mapping is approximated with the order N interpolation (see Eq. (20)), which is then differentiated to get the discrete covariant basis and Jacobian, $\mathcal{J}$. The contravariant basis, however, is computed using a curl form [50],

$$\mathcal{J}a_n^i = -\hat{x}^i \cdot \nabla_\xi \times \mathrm{I}^N\left(X_l \nabla_\xi X_m\right), \quad i,n = 1,2,3, \quad (n,m,l) \text{ cyclic}, \tag{24}$$

to fulfill the *discrete metric identities* [50], key to ensure the free-stream preservation (i.e. the derivative of a constant is zero) on curvilinear grids.

To construct the scheme we first cast the PDE (11) as a second order system introducing the auxiliary variable $\vec{\mathbf{g}} = \nabla\mathbf{w}$, and transform the operators to the reference space,

$$\begin{aligned} J\mathbf{q}_t + \nabla_\xi\cdot\vec{\tilde{\mathbf{f}}}_e(\mathbf{q}) &= \nabla_\xi\cdot\vec{\tilde{\mathbf{f}}}_v\left(\mathbf{q},\vec{\mathbf{g}}\right) + J\mathbf{s}\left(\mathbf{q},\vec{\mathbf{g}}\right), \\ J\vec{\mathbf{g}} &= \mathcal{M}\nabla_\xi\mathbf{w}. \end{aligned} \tag{25}$$

Next, we multiply Eq. (25) by two order N polynomial arbitrary test functions, integrate over the reference element E, and apply the Gauss law on the inviscid and viscous fluxes, and on the gradient of $\mathbf{w}$,

$$\begin{aligned} &\langle J\mathbf{q}_t,\boldsymbol{\phi}\rangle_E + \int_{\partial e}\boldsymbol{\phi}^T\left(\vec{\mathbf{f}}_e - \vec{\mathbf{f}}_v\right)\cdot \mathrm{d}\vec{S} - \left\langle\vec{\tilde{\mathbf{f}}}_e, \nabla_\xi\boldsymbol{\phi}\right\rangle_E = \\ &\quad -\left\langle\vec{\tilde{\mathbf{f}}}_v, \nabla_\xi\boldsymbol{\phi}\right\rangle_E + \langle J\mathbf{s},\boldsymbol{\phi}\rangle_E, \\ &\left\langle J\vec{\mathbf{g}},\vec{\boldsymbol{\varphi}}\right\rangle_E = \int_{\partial e}\mathbf{w}^T\vec{\boldsymbol{\varphi}}\cdot\mathrm{d}\vec{S} - \left\langle\mathbf{w},\nabla_\xi\cdot\vec{\boldsymbol{\varphi}}\right\rangle_E. \end{aligned} \tag{26}$$

Now we replace the polynomial ansatz. The functions are approximated by polynomials, and the integrals by quadratures. As a result of the disconnection between adjacent elements, the solution can be discontinuous across the inter-element faces, and the fluxes at the surface integrals are not defined. Thus, we use a uniquely defined *numerical flux* at the surface integrals, $\vec{\mathbf{f}} \approx \vec{\mathbf{f}}^\star\left(\mathbf{q}_\mathrm{L},\mathbf{q}_\mathrm{R}\right)$ that depend on the two neighboring states,

$$\begin{aligned} &\langle J\mathbf{Q}_t,\boldsymbol{\phi}\rangle_{E,N} + \int_{\partial e,N}\boldsymbol{\phi}^T\left(\vec{\mathbf{F}}_e^\star - \vec{\mathbf{F}}_v^\star\right)\cdot\mathrm{d}\vec{S} - \left\langle\vec{\tilde{\mathbf{F}}}_e,\nabla_\xi\boldsymbol{\phi}\right\rangle_{E,N} = \\ &\quad -\left\langle\vec{\tilde{\mathbf{F}}}_v,\nabla_\xi\boldsymbol{\phi}\right\rangle_{E,N} + \langle J\mathbf{S},\boldsymbol{\phi}\rangle_{E,N}, \\ &\left\langle J\vec{\mathbf{G}},\vec{\boldsymbol{\varphi}}\right\rangle_{E,N} = \int_{\partial e,N}\mathbf{W}^{\star,T}\vec{\boldsymbol{\varphi}}\cdot\mathrm{d}\vec{S} - \left\langle\mathbf{W},\nabla_\xi\cdot\vec{\boldsymbol{\varphi}}\right\rangle_{E,N}. \end{aligned} \tag{27}$$

Lastly, we enhance the robustness of this implementation by using a split-form scheme [54,68]. To do so, we apply again the Gauss law on the inviscid fluxes,

$$\begin{aligned} &\langle J\mathbf{Q}_t,\boldsymbol{\phi}\rangle_{E,N} + \int_{\partial e,N}\boldsymbol{\phi}^T\left(\vec{\mathbf{F}}_e^\star - \vec{\mathbf{F}}_e - \vec{\mathbf{F}}_v^\star\right)\cdot\mathrm{d}\vec{S} + \left\langle\mathbb{D}\left(\vec{\mathbf{F}}_e\right),\boldsymbol{\phi}\right\rangle_{E,N} = \\ &\quad -\left\langle\vec{\tilde{\mathbf{F}}}_v,\nabla_\xi\boldsymbol{\phi}\right\rangle_{E,N} + \langle J\mathbf{S},\boldsymbol{\phi}\rangle_{E,N}, \\ &\left\langle J\vec{\mathbf{G}},\vec{\boldsymbol{\varphi}}\right\rangle_{E,N} = \int_{\partial e,N}\mathbf{W}^{\star,T}\vec{\boldsymbol{\varphi}}\cdot\mathrm{d}\vec{S} - \left\langle\mathbf{W},\nabla_\xi\cdot\vec{\boldsymbol{\varphi}}\right\rangle_{E,N}, \end{aligned} \tag{28}$$

where $\mathbb{D}\left(\vec{\mathbf{F}}_e\right)$ is a split-form approximation of the divergence $\nabla_\xi\cdot\vec{\mathbf{F}}_e$ that uses a two-point flux $\vec{\mathbf{F}}_e^\#$,

$$\begin{aligned} \mathbb{D}\left(\vec{\mathbf{F}}_e\right)_{ijk} = 2\sum_{m=0}^{N}\Big(&D_{im}\vec{\tilde{\mathbf{F}}}_e\left(\mathbf{Q}_{ijk},\mathbf{Q}_{mjk}\right) + D_{jm}\vec{\tilde{\mathbf{G}}}_e\left(\mathbf{Q}_{ijk},\mathbf{Q}_{imk}\right) \\ &+ D_{km}\vec{\tilde{\mathbf{H}}}_e\left(\mathbf{Q}_{ijk},\mathbf{Q}_{ijm}\right)\Big), \end{aligned} \tag{29}$$

with $D_{ij} = l_j'\left(\xi_i\right)$. For this work, we adapt the two-point flux derived in [59] for the incompressible Navier–Stokes to the system solved herein. For the last four equations we simply copy the two-point flux from [59], and then we perform the product of the averages for the first two equations:

$$\vec{\mathbf{F}}_e^\# = \begin{pmatrix} \{\{c_1\}\}\{\{u\}\} & \{\{c_1\}\}\{\{v\}\} & \{\{c_1\}\}\{\{w\}\} \\ \{\{c_2\}\}\{\{u\}\} & \{\{c_2\}\}\{\{v\}\} & \{\{c_2\}\}\{\{w\}\} \\ \{\{\rho\}\}\{\{u\}\}^2 + \{\{p\}\} & \{\{\rho\}\}\{\{u\}\}\{\{v\}\} & \{\{\rho\}\}\{\{u\}\}\{\{v\}\} \\ \{\{\rho\}\}\{\{u\}\}\{\{v\}\} & \{\{\rho\}\}\{\{v\}\}^2 + \{\{p\}\} & \{\{\rho\}\}\{\{v\}\}\{\{w\}\} \\ \{\{\rho\}\}\{\{u\}\}\{\{w\}\} & \{\{\rho\}\}\{\{v\}\}\{\{w\}\} & \{\{\rho\}\}\{\{w\}\}^2 + \{\{p\}\} \\ \rho_0 c_0^2\{\{u\}\} & \rho_0 c_0^2\{\{v\}\} & \rho_0 c_0^2\{\{w\}\} \end{pmatrix}, \tag{30}$$

$$\vec{\mathbf{F}}_{e,i}^\# = \{\{\mathcal{M}\}\}\vec{\mathbf{F}}_{e,i}^\#,$$

where the brackets represent the average between the two states,

$$\{\{u\}\} = \frac{u_i + u_m}{2}. \tag{31}$$

The approximation of the equations is completed with the approximation of the chemical potentials, which are the first two gradient variables w_1, w_2. To do so, we proceed as in the PDE: we cast the definition of the chemical potentials introducing auxiliary variables $\vec{g}_{c,i} = \nabla c_i$, we transform the differential operators to the reference space, we construct weak forms within the elements, and integrate the volume terms with differential operators to get,

$$\begin{aligned}\langle \mathcal{J}\mu_i, \phi\rangle_{E,N} &= \left\langle \mathcal{J}\frac{12}{\epsilon}\Sigma_i F_i, \phi\right\rangle_{E,N} - \frac{3}{4}\epsilon\Sigma_i \int_{\partial e,N} \phi\left(\vec{G}^{\star}_{c,i}\right)\cdot \mathrm{d}\vec{S} \\ &\quad + \frac{3}{4}\epsilon\Sigma_i \left\langle \vec{\tilde{G}}_{c,i}, \vec{\nabla}_{\xi}\phi\right\rangle_{E,N}, \\ \left\langle \mathcal{J}\vec{G}_{c,i}, \vec{\varphi}\right\rangle_{E,N} &= \int_{\partial e,N} C_i^{\star,T}\vec{\varphi}\cdot \mathrm{d}\vec{S} - \left\langle C_i, \vec{\nabla}_{\xi}\cdot\vec{\tilde{\varphi}}_{G_c}\right\rangle_{E,N}.\end{aligned} \tag{32}$$

From the concentration field (C_1, C_2), we compute the chemical potentials (μ_1, μ_2), which are then introduced in the gradient variables $\mathbf{W}$, to compute their gradient $\vec{\mathbf{G}}$, and the state vector time derivative $\mathbf{Q}_t$. In the next sections, we describe the computation of the numerical fluxes for inter-element and physical boundary faces.

3.1.1. Numerical fluxes

The numerical fluxes couple the inter-element solutions through an uniquely defined value for the surface integrals. For the inviscid Riemann solver $\vec{\mathbf{F}}^{\star}_e$ we compute the exact Riemann problem solution derived in [69] for the normal velocity $u^{\star}$ and the pressure $p^{\star}$,

$$\begin{aligned}u^{\star} &= \frac{p_R - p_L + \rho_R u_R \lambda_R^- - \rho_L u_L \lambda_L^+}{\rho_R\lambda_R^- - \rho_L\lambda_L^+}, \quad p^{\star} = p_R + \rho_R\lambda_R^-(u_R - u^{\star}), \\ c_1^{\star}, c_2^{\star}, v^{\star}, w^{\star} &= \begin{cases} c_{1L}, c_{2L}, v_L, w_L & \text{if} \quad u^{\star} \geqslant 0 \\ c_{1R}, c_{2R}, v_R, w_R & \text{if} \quad u^{\star} < 0 \end{cases},\end{aligned} \tag{33}$$

and we compute the tangential velocities $v^{\star}, w^{\star}$ and concentrations $c_1^{\star}, c_2^{\star}$ from the appropriate element depending on the sign of $u^{\star}$. The eigenvalues $\lambda^{\pm}$ are $\lambda^{\pm} = (u \pm a)/2$, with $a = \sqrt{u^2 + 4\rho_0 c_0^2/\rho}$. Among the beneficial properties of this Riemann solver, we highlight that it is physical (it is the exact solution of the Riemann problem), efficient (e.g. does not need any iterative solution) and parameter-free.

For viscous fluxes and gradient variables, $\vec{\mathbf{F}}^{\star}_v$ and $\mathbf{W}^{\star}$, we use the Symmetric Interior Penalty (SIP) method,

$$\mathbf{W}^{\star} = \{\{\mathbf{W}\}\}, \quad \vec{\mathbf{F}}^{\star}_v = \left\{\left\{\vec{\mathbf{F}}_v\left(\mathbf{Q}, \vec{\nabla}\mathbf{W}\right)\right\}\right\} + \beta \begin{pmatrix} \frac{M_0}{\Sigma_1}[\![\mu_1]\!] \\ \frac{M_0}{\Sigma_2}[\![\mu_2]\!] \\ \frac{\eta}{\min(\rho_1,\rho_2)}[\![\rho\vec{u}]\!] \\ 0 \end{pmatrix}\vec{n}_L, \tag{34}$$

which uses the local gradient (23) for $\vec{\nabla}\mathbf{W}$. We take the penalty parameter from [70]

$$\beta = \frac{(N+1)(N+2)}{2\bar{h}}, \quad \bar{h} = \frac{\min\left(V_L, V_R\right)}{S}, \tag{35}$$

where $\bar{h}$ yields an approximated measure of the minimum element size normal to the face, V_L and V_R are the volumes of the neighboring elements, and S is the area of the face. Finally, for the concentration and its gradient we also use the SIP method,

$$C_i^{\star} = \{\{C_i\}\}, \quad \vec{G}^{\star}_{c,i} = \left\{\left\{\vec{\nabla}C_i\right\}\right\} - \beta\left(C_{i,L}\vec{n}_L + C_{i,R}\vec{n}_R\right). \tag{36}$$

3.2. Time discretization

The fourth order spatial derivative in the Cahn–Hilliard equation is too stiff to be solved explicitly for arbitrary values of the mobility parameter. Unless the mobility is low enough to allow reasonable time-steps, we use an IMplicit–EXplicit (IMEX) method to integrate in time: Navier–Stokes terms are solved using a third-order explicit Runge–Kutta (RK3) method, the Cahn–Hilliard chemical free-energy is solved using forward Euler and the Cahn–Hilliard interface energy is solved using backward Euler. Low-storage Runge–Kutta schemes are widespread within the high-order methods community since they yield high-order approximations with minimal computational storage requirements [34]. This first-order IMEX scheme was adapted from that derived in [28] in the context of N-phase flows.

This IMEX procedure has two steps, which we describe in a semi-discrete fashion (continuous in space, discrete in time):

1. We perform the explicit RK3 step for the Navier–Stokes terms, without the contribution from the chemical-free energy and interfacial energy in the Cahn–Hilliard equation,

$$\begin{pmatrix} c_1 \\ c_2 \\ \rho\vec{u} \\ p \end{pmatrix}_t = -\nabla\cdot\begin{pmatrix} c_1\vec{u} \\ c_2\vec{u} \\ \rho\vec{u}\vec{u} + p\mathrm{I}_3 \\ \rho_0 c_0^2\vec{u} \end{pmatrix} + \nabla\cdot\begin{pmatrix} 0 \\ 0 \\ \eta\left(\nabla\vec{u} + \nabla\vec{u}^T\right) \\ 0 \end{pmatrix} + \begin{pmatrix} 0 \\ 0 \\ \rho\vec{g} + \sum_{m=1}^{3}\mu_m\nabla c_m \\ 0 \end{pmatrix}. \tag{37}$$

   After the RK3 time-step, the variables are called $\left(\hat{c}_1, \hat{c}_2, \rho\vec{u}^{n+1}, p^{n+1}\right)$, since the concentrations need a correction step to include the chemical potential.
2. We compute a correction step on the two concentrations to solve the Cahn–Hilliard equations. The chemical free-energy terms are solved explicitly (i.e. evaluated in c_i^n) and the stiff interfacial energy terms implicitly (i.e. evaluated in c_i^{n+1}). Besides, we also introduce the stabilizing term $S_0\left(c_i^{n+1} - c_i^n\right)$, being S_0 a constant. The stabilization term is a widely used technique to make possible the approximation of the non-linear terms of the chemical potential explicitly, while maintaining the higher time-step sizes of an implicit scheme. The reasoning behind the selection of S_0 is the smallest possible such that the system is stable. Throughout this work, and in other related works [62], the value $S_0 = 8$, which was found by trial-and-error, has provided successful solutions. Finally, the approximation of the time derivative is $c_{i,t} \approx \left(c_i^{n+1} - \hat{c}_i\right)/\Delta t$. As a result, the IMEX correction step for each concentration is:

$$\frac{c_i^{n+1} - \hat{c}_i}{\Delta t} = M_0\vec{\nabla}^2\left(\frac{12}{\epsilon}f_i(c_1^n, c_2^n, c_3^n) + S_0\left(c_i^{n+1} - c_i^n\right) - \frac{3}{4}\epsilon\vec{\nabla}^2 c_i^{n+1}\right). \tag{38}$$

   Two decoupled linear systems for the two concentration parameters are solved. However, the linearity of the operator produces a constant in time Jacobian, which also is identical for both phases. These properties led us to compute the solution to the linear problem with LU factorization (performed only once at the preprocessing) and Gauss substitution. The computational cost of the latter is similar to an iteration in a explicit method.

3.3. Boundary conditions

In this section we describe the imposition of inflow, outflow, and no-slip wall boundary conditions. In this work, we prescribe the boundary conditions weakly. Hence, we create a ghost (exterior) state with the appropriate boundary information, and then compute the interface fluxes between the interior $\mathbf{Q}^i$ and exterior $\mathbf{Q}^e$ states.

3.3.1. Inflow boundary condition

For the inflow boundary condition, we specify the inflow concentration $c_{i,\mathrm{inflow}}(\vec{x};t)$ and the velocity $\vec{u}_{\mathrm{inflow}}\left(\vec{x};t\right)$. For the inviscid fluxes, we construct a ghost state,

$$\mathbf{Q}^e = \begin{pmatrix} C_{1,\mathrm{inflow}} \\ C_{2,\mathrm{inflow}} \\ \rho\left(C_{\mathrm{inflow}}\right)\vec{U}_{\mathrm{inflow}} \\ P \end{pmatrix}, \tag{39}$$

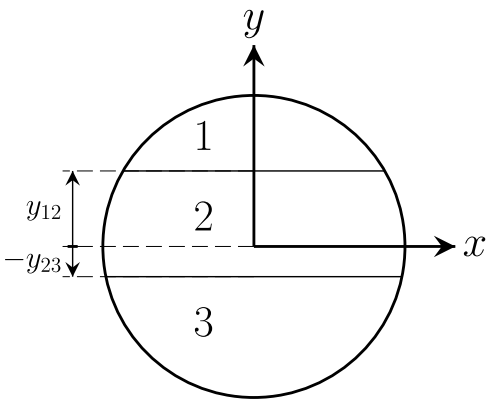

Fig. 2. Configuration of a layered inflow. The position of the two interfaces is provided by the values y_{12} and y_{23}.

where we take the pressure P from the interior, and compute the interface flux from the exact Riemann problem solution (see Eqs. (33)), $\vec{\mathbf{F}}_e^\star\left(\mathbf{Q}_e^i, \mathbf{Q}_e^e\right)$.

We define the viscous fluxes as:

$$\mathbf{W}^\star = \frac{\mathbf{W}^i + \mathbf{W}^e}{2}, \quad \mathbf{F}_v^\star \cdot \vec{n} = \begin{pmatrix} 0 \\ 0 \\ \eta\left(\nabla\vec{U} + \nabla\vec{U}^T\right)\cdot\vec{n} \\ 0 \end{pmatrix}, \tag{40}$$

where we apply the Neumann boundary conditions to the chemical potential, and take the interior values for viscous stresses. In (40), we compute the gradient variables from the ghost state, $\mathbf{W}^e = \mathbf{W}(\mathbf{Q}^e)$.

The implementation features an automatic method for the distribution of the phases in a circular section, given the superficial velocities and the slip velocities. The superficial velocity of each phase is, for a given flow rate, the equivalent velocity obtained if the phase occupies the entire section,

$$v_{s,i} = \frac{1}{A_{\text{inflow}}}\int_{\text{inflow}} \vec{u}_i \cdot \mathrm{d}\vec{S}. \tag{41}$$

Furthermore, because real flow configurations feature a large ratio of the superficial velocities that confine one of the phases to the near wall region, we allow the velocity to be discontinuous at the interface between the phases. By doing so, we can use lower velocities for the phases with smaller superficial velocity, so that they occupy a larger region of the cross section. The problem with a phase being very confined to the near wall region is that it might not be well captured by the numerical method. For the flow configuration given in Fig. 2, the concentration inflow boundary condition is

$$\begin{aligned} c_{1,\text{inflow}}(x,y) &= \frac{1}{2} + \frac{1}{2}\tanh\left(\frac{y-y_{12}}{\varepsilon}\right), \\ c_{2,\text{inflow}}(x,y) &= \frac{1}{2}\tanh\left(\frac{y-y_{23}}{\varepsilon}\right) - \frac{1}{2}\tanh\left(\frac{y-y_{12}}{\varepsilon}\right), \end{aligned} \tag{42}$$

and the velocities are computed from a Poiseuille flow,

$$u_{\text{inflow}} = \left(V_{1,\max}c_{1,\text{inflow}} + V_{2,\max}c_{2,\text{inflow}} + V_{3,\max}c_{3,\text{inflow}}\right)\left(1 - \left(\frac{r}{R}\right)^2\right), \tag{43}$$

with the two slip velocities, which are user-input,

$$V_{s,12} = V_{1,\max} - V_{2,\max}, \quad V_{s,23} = V_{2,\max} - V_{3,\max}. \tag{44}$$

Therefore, there are five unknowns ($V_{1,\max}$, $V_{2,\max}$, $V_{3,\max}$, y_{12}, and y_{23}), and five equations: the two slip-velocities definitions (see Eq. (44)), and the superficial velocities,

$$v_{s,i} = \frac{V_{i,\max}}{A_{\text{inflow}}}\int_{\text{inflow}} c_{i,\text{inflow}}\left(1 - \left(\frac{r}{R}\right)^2\right)\mathrm{d}S, \tag{45}$$

that are solved using a Newton–Raphson method.

3.3.2. Outflow boundary condition

The outflow boundary condition specifies the ambient pressure at the exit of the domain P_o, and applies a Neumann boundary condition to the rest of the variables. Therefore, for the inviscid fluxes the exterior state is defined as:

$$\mathbf{Q}^e = \begin{pmatrix} C_1 \\ C_2 \\ \rho\vec{U} \\ P_o \end{pmatrix}, \tag{46}$$

whereas for viscous fluxes we simply use a Neumann boundary condition for all the variables,

$$\mathbf{W}^\star = \mathbf{W}_i, \quad \mathbf{F}_v^\star \cdot \vec{n} = 0. \tag{47}$$

3.3.3. No-slip wall boundary condition

We construct a ghost state with the same variables as the inside, but changing the sign of the normal velocity,

$$\mathbf{Q}^e = \begin{pmatrix} c_1 \\ c_2 \\ \rho\left(\vec{U} - 2\left(\vec{U}\cdot\vec{n}\right)\vec{n}\right) \\ p \end{pmatrix}. \tag{48}$$

For the viscous numerical fluxes, we apply Neumann boundary conditions in all variables except velocities, which take the interior values,

$$\mathbf{W}^\star = \frac{\mathbf{W}^i + \mathbf{W}^e}{2}, \quad \vec{\mathbf{F}}_v^\star \cdot \vec{n} = \begin{pmatrix} 0 \\ 0 \\ \eta\left(\nabla\vec{U} + \nabla\vec{U}^T\right)\cdot\vec{n} \\ 0 \end{pmatrix}. \tag{49}$$

Finally, for the gradient of the concentrations $\vec{G}_{c,i}^\star$ the Neumann boundary condition is non-homogeneous, if one wants to solve for arbitrary wall contact angles. Thus, we follow [62,71] and use the following expression:

$$C_i^\star = C_i, \quad \vec{G}_{c,i}^\star \cdot \vec{n} = F_{w,i}, \tag{50}$$

where the boundary coefficients $F_{w,i}$ are

$$\begin{aligned} F_{w,1} &= -\frac{4}{\varepsilon}\left(\cos\theta_{12}^w C_1 C_2\left(C_1 + C_2\right) + \cos\theta_{13}^w C_1 C_3\left(C_1 + C_3\right)\right), \\ F_{w,2} &= -\frac{4}{\varepsilon}\left(-\cos\theta_{12}^w C_1 C_2\left(C_1 + C_2\right) + \cos\theta_{23}^w C_2 C_3\left(C_1 + C_3\right)\right), \end{aligned} \tag{51}$$

being the three wall contact angles θ_{ij}^w related by the wall equilibrium constraint [62,71],

$$\sigma_{12}\cos\theta_{12}^w + \sigma_{23}\cos\theta_{23}^w = \sigma_{13}\cos\theta_{13}^w.$$

For 90° angles, the coefficients $F_{w,i}$ are zero, and the boundary condition reduces to the homogeneous Neumann boundary condition.

4. Results

In this section, we perform the validation of the approach proposed. First, we solve a manufactured solution to verify the three-phase solver accuracy. Then, a validation is conducted for a two-phase horizontal pipe. Finally, a three-phase T-shaped pipe intersection is simulated.

4.1. Manufactured solution

First, we study the convergence properties of the method. To do this, we extend the two-dimensional the manufactured solution presented in [43] to the manufactured solution of the three-phase Cahn–Hilliard solver.

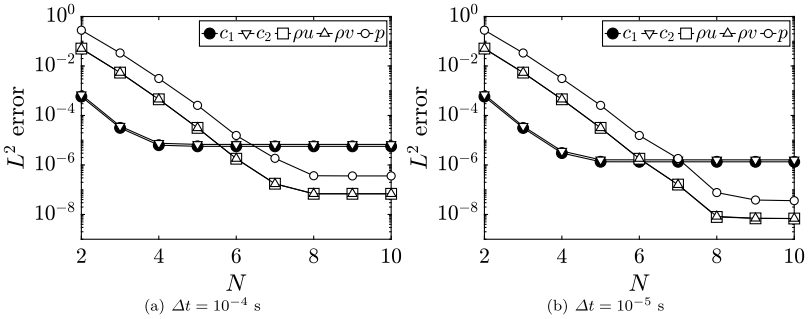

Fig. 3. Three-phase solver: polynomial order convergence study of the manufactured solution (52). We represent the L^2 errors of the two concentrations c_1 and c_2, x- and y-momentum, and pressure. The polynomial order ranges from 2 to 10, and we integrate in time until $t_F = 0.1$ s with two time step sizes: $\Delta t = 10^{-4}$ s and 10^{-5} s. All physical parameters are given in Table 1.

Table 1
Three-phase solver: list of the parameter values used in the manufactured solution (see Eq. (52)).

ρ_1	ρ_2	ρ_3 (kg/m^3)	η_1	η_2	η_3 (Pa s)	ϵ (m)
1.0	3.0	2.0	1.0E−3	1.0E−3	1.0E−3	$1/\sqrt{2}$
	M_0 (m/s)	c_0^2 (m/s)^2	σ_{12}	σ_{13}	σ_{23} (N/m)	
	1.134E−2	1.0E3	6.236E−3	7.265E−3	8.165E−3	

As a result, the three-phase manufactured solution is defined as:

$$
\begin{aligned}
c_{1,0}(x,y;t) &= \frac{1}{3}\left(1+\cos(\pi x)\sin(\pi y)\sin(t)\right),\\
c_{2,0}(x,y;t) &= \frac{1}{3}\left(1+\cos(\pi x)\sin(\pi y)\sin(1.2t)\right),\\
u_0(x,y;t) &= 2\sin(\pi x)\cos(\pi z)\sin(t),\\
v_0(x,y;t) &= -2\cos(\pi x)\sin(\pi y)\sin(t),\\
p_0(x,y;t) &= 2\sin(\pi x)\sin(\pi z)\cos(t),
\end{aligned}
\tag{52}
$$

which requires an appropriate balancing source term, not presented here for simplicity. We solve it on the domain $(x, y) \in [-1, 1]^2$ m. The final time is $t_F = 0.1$ s, and all the physical parameters have been adapted from [28] and they are given in Table 1.

First, we perform a polynomial order convergence study on a Cartesian mesh of 4^2 elements, and with the polynomial order ranging from $N = 2$ to 10. In Fig. 3 we represent the L^2 errors on the five variables (c_1, c_2, ρu, ρv and p) at the final time $t_F = 0.1$ s, for two time-step sizes, $\Delta t = 10^{-4}$ s and 10^{-5} s. Regarding the error behavior, an exponential accuracy is obtained for lower polynomial order, as expected, and then the error stagnation associated with the time discretization is anticipated for the two concentrations, as a result of the first-order IMEX scheme.

Finally, we perform the mesh convergence study, where we use meshes with 4^2, 6^2, 8^2, 12^2 and 16^2 elements, and vary the polynomial order from $N = 2$ to $N = 5$. The L^2 errors and the convergence rates are written in Table 2. We observe that for the two concentrations the convergence rates are always between N and $N + 2$, for $N = 2$ and $N = 3$, and due to the early stagnation, we cannot evaluate the convergence rates for $N = 4$ and $N = 5$. For the rest of the variables, we find that the convergence rates are always between N and $N + 1$, as expected. As previously mentioned, note that high-order three-dimensional industrial CFD simulations typically use $N = 2, 3$, to keep a balance between accuracy and cost.

Overall, we confirm that the scheme and its implementation are accurate for industrial applications.

4.2. Two-phase pipe simulations

In this section, we focus on a test case relevant for the oil and gas industry. In particular, we simulate the flow in horizontal pipes

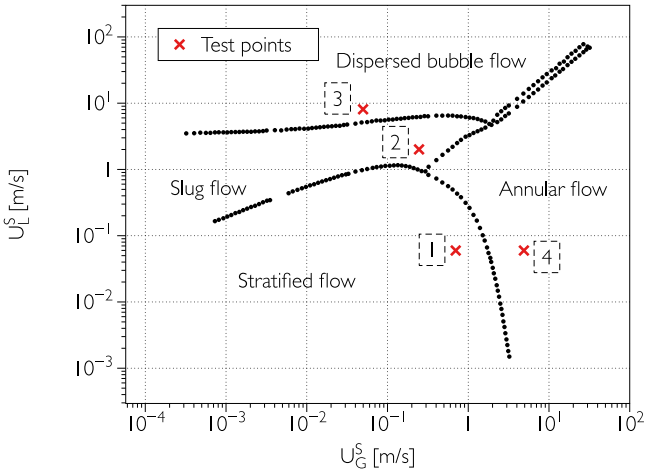

Fig. 4. Two-phase solver: flow pattern map of the two-phase flow in a horizontal pipe with a diameter of 1 meter.
Source: The data has been extracted from [72].

with different superficial velocities (see Eq. (45)) at the inflow, U_G^S and U_L^S, which correspond to the gas and liquid respectively. Depending on the superficial velocities values, we obtain different flow regimes. This test case follows the one proposed in [42,72] and agrees with the experimental results of [73].

The flow pattern map of Taitel & Dukler (see Fig. 4) classifies the flow regimes as stratified flow, slug flow, dispersed bubble flow and annular flow. In a stratified flow the phases are completely separated with gas in the upper part and liquid in the lower part of the pipe. In a slug flow, the waves in the flow reach the top of the pipe, eventually closing the gas path at the top. In a dispersed bubble flow, small bubbles are present in the flow, and are dispersed everywhere in the cross section. In an annular flow, the liquid forms a coat all around the pipe walls. Following [72], we define four test cases that reproduce the four flow regimes, denoted with red crosses in Fig. 4, and whose superficial velocities are given in Table 3. The domain for the simulations consists of a pipe with length $L = 1$ m and diameter $D = 0.1$ m. The physical domain is discretized using a mesh of 8220 hexahedral elements and the solution is approximated by order $N = 3$ polynomials. The physical parameters are summarized in Table 4. The mobility is taken from [72], and the width of the interface covers approximately three points in the high-order mesh. The time step chosen for the simulations is $\Delta t = 10^{-5}$ s. Regarding the boundary conditions, a no-slip boundary condition (see Eq. (48)) is enforced at the pipe walls (with a contact angle of 90°) while a velocity inflow boundary condition (see Eq. (39)) and a constant pressure outflow boundary condition (see Eq. (46)) are used. It should be noted that the flow regime inflow is

Table 2
Three-phase solver: manufactured solution (see Eq. (52)) convergence analysis: we use 4^3, 8^3, and 16^3 meshes, and $N = 2, 3, 4$ and 5. The final time is $t_F = 0.1$ s, and we use the IMEX scheme with $\Delta t = 5 \cdot 10^{-5}$ s.

	Mesh	c_1 error	Order	c_2 error	Order	ρu error	Order	ρv error	Order	p error	Order
N = 2	4^2	5.82E−04	–	6.97E−04	–	5.06E−02	–	5.06E−02	–	2.81E−01	–
	6^2	1.60E−04	3.19	1.91E−04	3.19	1.92E−02	2.39	1.92E−02	2.39	1.17E−01	2.15
	8^2	5.97E−05	3.42	7.15E−05	3.41	9.38E−03	2.49	9.38E−03	2.49	6.19E−02	2.22
	12^2	1.61E−05	3.23	1.93E−05	3.23	3.28E−03	2.59	3.28E−03	2.59	2.40E−02	2.34
	16^2	6.65E−06	3.07	7.97E−06	3.07	1.51E−03	2.70	1.51E−03	2.70	1.18E−02	2.47
N = 3	4^2	3.13E−05	–	3.69E−05	–	5.41E−03	–	5.41E−03	–	3.36E−02	–
	6^2	3.67E−06	5.29	4.38E−06	5.26	1.30E−03	3.52	1.30E−03	3.52	9.41E−03	3.14
	8^2	1.49E−06	3.13	1.79E−06	3.11	4.51E−04	3.68	4.50E−04	3.68	3.65E−03	3.30
	12^2	1.35E−06	0.25	1.62E−06	0.25	9.55E−05	3.83	9.55E−05	3.83	9.01E−04	3.45
	16^2	1.35E−06	0.00	1.61E−06	0.00	3.08E−05	3.94	3.08E−05	3.94	3.20E−04	3.60
N = 4	4^2	3.03E−06	–	3.65E−06	–	4.52E−04	–	4.52E−04	–	3.12E−03	–
	6^2	1.39E−06	1.93	1.66E−06	1.94	7.10E−05	4.56	7.10E−05	4.57	5.47E−04	4.30
	8^2	1.35E−06	0.10	1.62E−06	0.10	1.85E−05	4.67	1.85E−05	4.67	1.52E−04	4.46
	12^2	1.35E−06	0.00	1.61E−06	0.00	2.67E−06	4.77	2.67E−06	4.77	2.37E−05	4.58
	16^2	1.35E−06	0.00	1.61E−06	0.00	6.59E−07	4.87	6.59E−07	4.87	6.20E−06	4.67
N = 5	4^2	1.35E−06	–	1.62E−06	–	3.17E−05	–	3.15E−05	–	2.57E−04	–
	6^2	1.35E−06	0.01	1.61E−06	0.01	3.18E−06	5.67	3.18E−06	5.66	2.83E−05	5.44
	8^2	1.35E−06	0.00	1.61E−06	0.00	6.23E−07	5.67	6.22E−07	5.67	5.79E−06	5.52
	12^2	1.35E−06	0.00	1.61E−06	0.00	6.48E−08	5.58	6.47E−08	5.58	5.81E−07	5.67
	16^2	1.35E−06	0.00	1.61E−06	0.00	1.50E−08	5.08	1.50E−08	5.08	1.15E−07	5.62

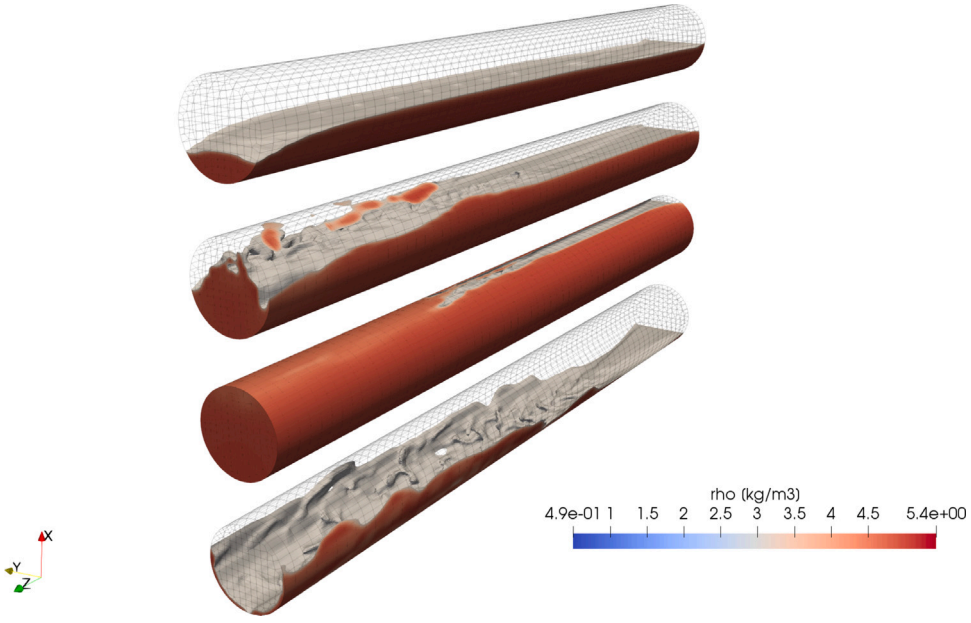

Fig. 5. Two-phase solver: results of test cases 1–4 (organized top to bottom) at $t = 4$s. Stratified, Slug, Dispersed Bubble and Annular Flow regimes.

Table 3
Two-phase solver: superficial velocities (in m/s) and theoretical flow regime in horizontal pipe test case.

Test	Flow regime	U_G^S	U_L^S
1	Stratified flow	0.7	0.06
2	Slug flow	0.25	2
3	Dispersed bubble flow	0.05	8
4	Annular flow	4.9	0.06

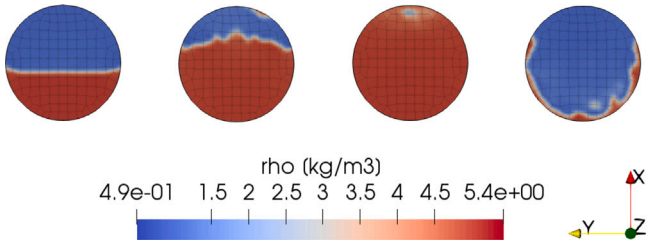

Fig. 6. Two-phase solver: representation of the density contour in a pipe at $z/D = 8$ cross section. The four regimes (stratified, slug, dispersed bubble, and annular) are represented.

considered layered (see Fig. 2). The initial condition for all simulations is propagated along the Z axis, with a small wave-like perturbation with Z coordinate, to introduce asymmetry.

Then, Fig. 5 shows an isosurface of c values under 0.5, colored by density, for the four test cases shown in Fig. 4 (organized from top to bottom from 1 to 4) at $t = 4$ s.

In Fig. 6 we show the density contour in a Z-normal slice at $L/D = 8$. As can be seen, the flow regimes are correctly predicted. Note that ignoring the effect of the hydrostatic pressure on the outlet when imposing a constant outlet pressure, it induces a velocity in the negative X direction that curves the interface. This can be more easily seen in the stratified flow regime (Test 1).

Table 4
Two-phase solver: physical parameters of the pipe flow.

ρ_1	ρ_2 (kg/m^3)	η_1	η_2 (Pa s)	ϵ (m)	M_0 (m/s)	c_0^2 (m/s)^2	σ (N/m)	g (m/s^2)
1.0	5.0	$5 \cdot 10^{-3}$	10^{-2}	0.0424	0.1886	1.0E3	$2.5 \cdot 10^{-4}$	1.0

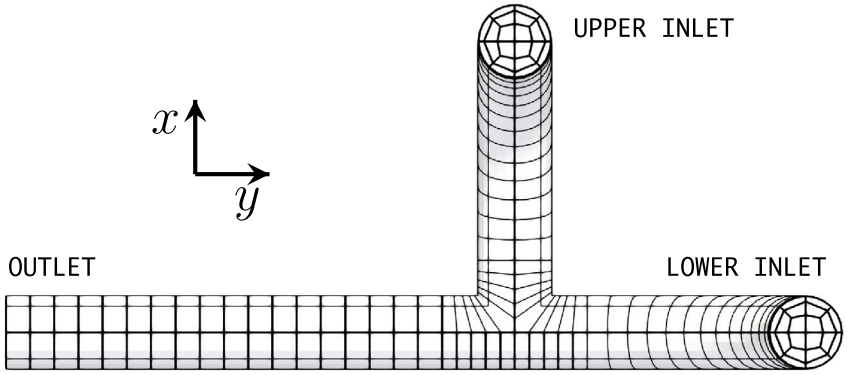

Fig. 7. Three-phase solver: computational mesh for the T-shaped junction pipe domain, with 1700 elements.

Table 5
Three-phase solver: list of the parameter values used for the three-phase T-shaped pipe intersection simulation.

ρ_1	ρ_2	ρ_3 (kg/m^3)	η_1	η_2	η_3 (Pa s)	ϵ (m)
5.0	1.0	0.2	1.0E−5	2.5E−5	5.0E−5	0.03
	M_0	c_0^2 (m/s)^2	σ_{12}	σ_{13}	σ_{23} (N/m)	g (m/s^2)
	1.8856E−2	1.0E3	2.5E−4	2.5E−4	2.5E−4	1.0

4.3. Three-phase T-shaped pipe intersection

Finally, we solve a T-shaped pipe junction configuration with two inlets and one outlet. The domain has a straight upper inlet whose length is 3 m, which is then coupled to a 90° bend whose radius is 3 m. Additionally, the second inlet has a straight 5 m section, and then another 90°/3 m bend. Finally, the outlet after the T-shaped junction is a straight pipe whose length is 6 m. The diameter of the pipe is $D = 1$ m. The computational mesh used has 1700 elements and is represented in Fig. 7.

Physical parameters are given in Table 5. In the upper inlet, we only inject phases 1 and 2 with superficial velocities $V_{s,1} = V_{s,2} = 4$ m/s. In the lower inlet, we only inject phase 3 with superficial velocity $V_{s,3} = 2$ m/s. Additionally, the gravity acceleration is $\vec{g} = -1$ m/s^2 in x-direction. We use a polynomial order $N = 3$, and the IMEX scheme uses $S_0 = 8$ with a time-step size $\Delta t = 5 \cdot 10^{-5}$ s. The initial condition is a steady state with uniform pressure $p = 0$, and with the pipe filled with phase 3 ($c_1 = c_2 = 0$).

We represent the evolution of the phases in Fig. 8, where we represent phase 2 in blue, phase 3 in gray and the space left is occupied by phase 1. Initially, the pipe is filled with phase 3, which was chosen because it has the minimum density of the three phases (so it is easier for the other two phases to displace it). At the initial stages (see Fig. 8(a)), we observe the advancing front at the upper inlet. We see that phase 2 (blue) overtakes phase 1 at the elbow, and then both phases arrive at the main pipe at $t \approx 1.5$ (see Fig. 8(b)). Then, phases 1 and 2 enter the principal pipe and restrict the flow of phase 3 after the T-shaped pipe intersection. The lower density fluid, phase 3, is then confined to the wall, and phases 1 and 2 intermittently occupy the bulk of the pipe (see Fig. 8(c)).

In Fig. 9 we represent the configuration of the three-phase at the final simulation time at $t = 7.5$ s. Both phases 1 (Fig. 9(a)) and 2 (Fig. 9(b)) represent the bulk of the pipe, whereas phase 3 (Fig. 9(c)) is forced to coat the walls of the pipe (similar to an annular flow regime). Due to the rupture of the flow of phase 3 by the phases 1 and 2, phase 3 gets a counter-clockwise swirl motion around the pipe.

Finally, we represent the velocity contours at the final time $t = 7.5$ s in Fig. 10. We can see the detachment due to the low viscosity of phase 2, at the upper elbow. A similar pattern is found at the lower elbow for phase 3. Then, after the T-shaped intersection, the flow becomes under-resolved, with large velocity spots, as a result of the interaction between the three phases.

Overall, we confirm the validity of the solver to compute simulations in complex three-dimensional geometries, as those found in the oil and gas industry.

5. Conclusions

We present a three-phase incompressible Navier–Stokes/Cahn–Hilliard system, and its discontinuous Galerkin implementation. The model uses the three-phase Cahn–Hilliard model of [17], and the incompressible Navier–Stokes with artificial compressibility of [59]. We construct a discontinuous Galerkin approximation of the equations, where we combine the scheme used for the three-phase Cahn–Hilliard model in [62] and that used for the kinetic-energy stable incompressible Navier–Stokes equations of [59]. An implicit–explicit (IMEX) method is adopted as temporal scheme for the Cahn–Hilliard equation, while Runge–Kutta 3 (RK3) is used for the Navier–Stokes equations. Therefore, the low-order temporal approximation is used exclusively to approximate the diffusive contribution of the Cahn–Hilliard equation, which is an artifact to simulate diffuse interfaces and phase separation. The interfaces produced by the Cahn–Hilliard equation will not

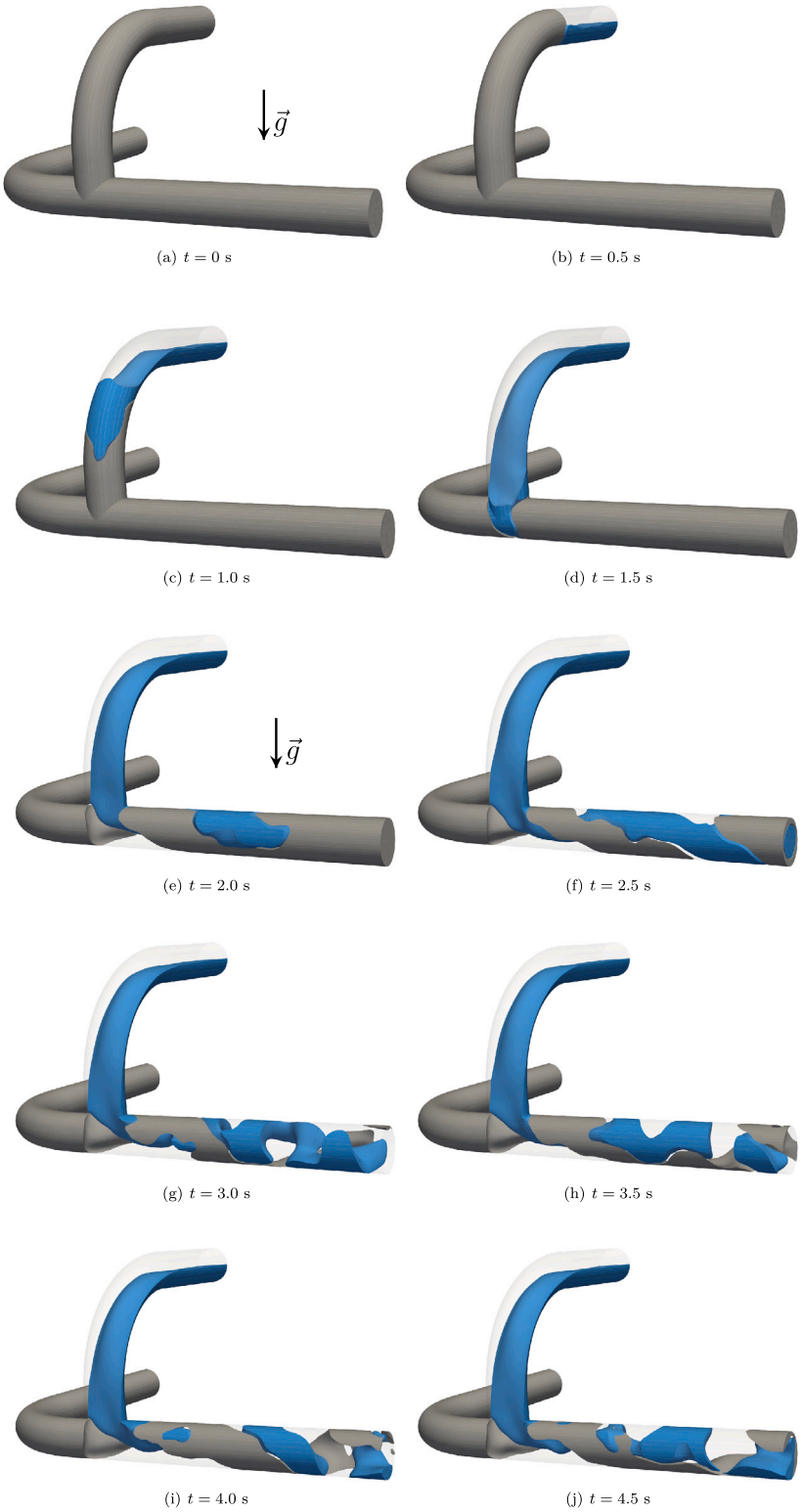

Fig. 8. Three-phase solver: evolution of phase two (blue) and phase three (gray) for the first 4.5 s.

be numerically diffused by the lower-order approximation, since the chemical free energy controls the sharpening back the interface. In the Navier–Stokes equations, however, the use of a high-order method has the advantage of a lower numerical dissipation, which prevents turbulent flow structures to quickly diffuse back into the flow.

First, the three-phase solver accuracy is validated with a manufactured solution test case. Then the numerical method is shown to correctly match a two-phase experimental flow regime map for a horizontal pipe. Finally, a three-dimensional T-shaped pipe intersection is solved as an example of a complex geometry. We highlight the ease in the configuration of the solver and the scheme for a user, as it

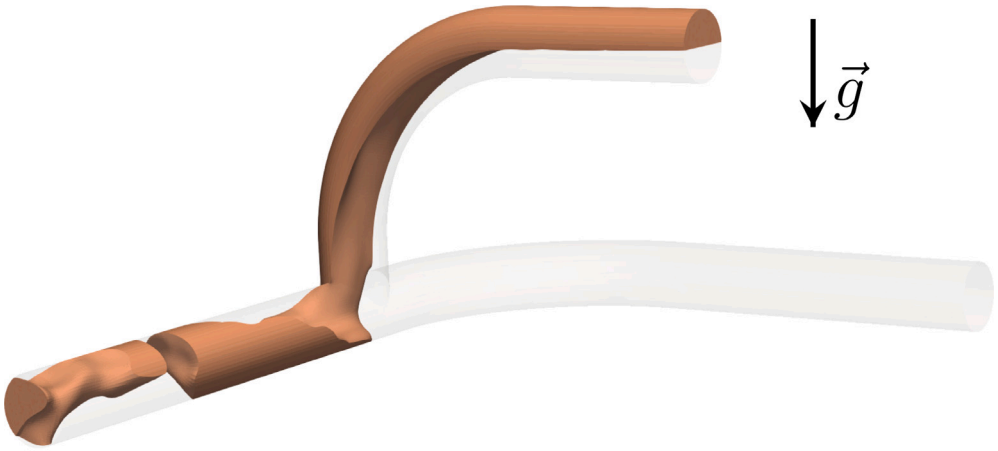

(a) Phase 1

(b) Phase 2

(c) Phase 3

Fig. 9. Three-phase solver: representation of the three-phase at the final time $t = 7.5$.

only requires an appropriate choice of the physical parameters and conditions, plus the choice of the polynomial order of the simulation. The rest of the numerical parameters have been proven valid in a vast range of flow conditions, and the boundary conditions are automatically set-up by the algorithm that computes the inlet profile for given superficial/slip velocities.

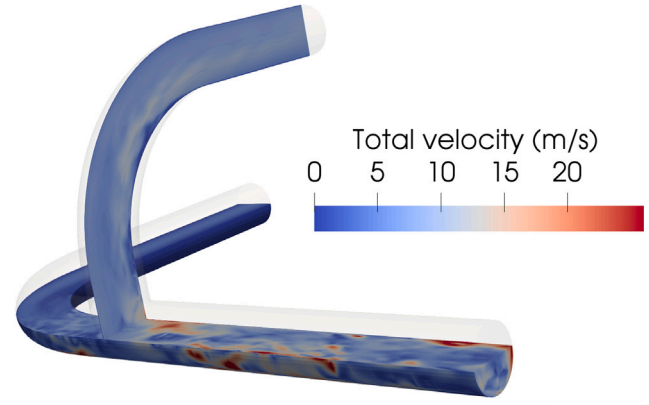

Fig. 10. Three-phase solver: total velocity contour at the final time $t = 7.5$ s.

CRediT authorship contribution statement

Juan Manzanero: Conceptualization, Methodology, Software, Validation, Formal analysis, Investigation, Data curation, Writing – original draft, Writing – review and editing, Visualization. **Carlos Redondo:** Conceptualization, Methodology, Software, Validation, Formal analysis, Investigation, Data curation, Writing – original draft, Writing – review and editing, Visualization. **Miguel Chávez-Módena:** Conceptualization, Methodology, Software, Validation, Formal analysis, Investigation, Data curation, Writing – original draft, Writing – review and editing, visualization. **Gonzalo Rubio:** Conceptualization, Methodology, Validation, Formal analysis, Investigation, Resources, Writing – original draft, Writing – review and editing, Supervision, Project administration, Funding acquisition. **Eusebio Valero:** Resources, Supervision, Project administration, Funding acquisition. **Susana Gómez-Álvarez:** Conceptualization, Resources, Supervision, Project administration, Funding acquisition. **Ángel Rivero-Jiménez:** Conceptualization, Methodology, Validation, Formal analysis, Investigation, Resources, Supervision, Project administration, Funding acquisition.

Declaration of competing interest

One or more of the authors of this paper have disclosed potential or pertinent conflicts of interest, which may include receipt of payment, either direct or indirect, institutional support, or association with an entity in the biomedical field which may be perceived to have potential conflict of interest with this work. For full disclosure statements refer to https://doi.org/10.1016/j.compfluid.2022.105545. Gonzalo Rubio reports financial support was provided by Repsol SA. Gonzalo Rubio reports was provided by Spain Ministry of Science and Innovation.

Acknowledgments

The authors acknowledge the computer resources and technical assistance provided by the Centro de Supercomputación y Visualización de Madrid (CeSViMa). The authors acknowledge Repsol Technology Lab and Universidad Politécnica de Madrid for their support and permission to publish this work. Gonzalo Rubio and Eusebio Valero acknowledge the funding received by the grant SIMOPAIR (Project No. REF: RTI2018-097075-B-I00) funded by MCIN/AEI/10.13039/501100011033 and by ERDF A way of making Europe. Authors also thank Gabriel Rucabado from Repsol Technology Lab for his assistance during the execution of this work.

References

[1] Belt R, Duret E, Larrey D, Djoric B, Kalali S, et al. Comparison of commercial multiphase flow simulators with experimental and field databases. In: 15th International conference on multiphase production technology. BHR Group; 2011.
[2] Gharaibah E, Read A, Scheuerer G, et al. Overview of CFD multiphase flow simulation tools for subsea oil and gas system design, optimization and operation. In: OTC Brasil. Offshore Technology Conference; 2015.
[3] Hirt CW, Nichols BD. Volume of fluid (VOF) method for the dynamics of free boundaries. J Comput Phys 1981;39(1):201–25.
[4] Sussman M, Smereka P, Osher S. A level set approach for computing solutions to incompressible two-phase flow. J Comput Phys 1994;114(1):146–59.
[5] Jacqmin D. Calculation of two-phase Navier–Stokes flows using phase-field modeling. J Comput Phys 1999;155(1):96–127.
[6] Anderson DM, McFadden GB, Wheeler AA. Diffuse-interface methods in fluid mechanics. Annu Rev Fluid Mech 1998;30(1):139–65.
[7] Badalassi VE, Ceniceros HD, Banerjee S. Computation of multiphase systems with phase field models. J Comput Phys 2003;190(2):371–97.
[8] Bonhomme R, Magnaudet J, Duval F, Piar B. Inertial dynamics of air bubbles crossing a horizontal fluid-fluid interface. 2012.
[9] Inoue Y, Chen Y, Ohashi H. A mesoscopic simulation model for immiscible multiphase fluids. J Comput Phys 2004;201(1):191–203.
[10] Merriman B, Bence JK, Osher SJ. Motion of multiple junctions: A level set approach. J Comput Phys 1994;112(2):334–63.
[11] Saye RI, Sethian JA. The Voronoi implicit interface method for computing multiphase physics. Proc Natl Acad Sci 2011;108(49):19498–503.
[12] Smith KA, Solis FJ, Chopp D. A projection method for motion of triple junctions by level sets. Interfaces Free Bound 2002;4(3):263–76.
[13] Villa A, Formaggia L. Implicit tracking for multi-fluid simulations. J Comput Phys 2010;229(16):5788–802.
[14] Zhao H-K, Chan T, Merriman B, Osher S. A variational level set approach to multiphase motion. J Comput Phys 1996;127(1):179–95.
[15] Zheng W, Yong J-H, Paul J-C. Visual simulation of multiple unmixable fluids. J Comput Sci Tech 2007;22(1):156–60.
[16] Zlotnik S, Díez P. Hierarchical X-FEM for n-phase flow (n> 2). Comput Methods Appl Mech Engrg 2009;198(30–32):2329–38.
[17] Boyer F, Lapuerta C. Study of a three component Cahn-Hilliard flow model. ESAIM Math Model Numer Anal 2006;40(4):653–87.
[18] Boyer F, Lapuerta C, Minjeaud S, Piar B, Quintard M. Cahn–Hilliard/Navier–Stokes model for the simulation of three-phase flows. Transp Porous Media 2010;82(3):463–83.
[19] Boyer F, Minjeaud S. Numerical schemes for a three component Cahn-Hilliard model. ESAIM Math Model Numer Anal 2011;45(4):697–738.
[20] Kim J. Phase field computations for ternary fluid flows. Comput Methods Appl Mech Engrg 2007;196(45–48):4779–88.
[21] Kim J. A generalized continuous surface tension force formulation for phase-field models for multi-component immiscible fluid flows. Comput Methods Appl Mech Engrg 2009;198(37–40):3105–12.
[22] Kim J. Phase-field models for multi-component fluid flows. Commun Comput Phys 2012;12(3):613–61.
[23] Kim J, Kang K, Lowengrub J, et al. Conservative multigrid methods for ternary Cahn-Hilliard systems. Commun Math Sci 2004;2(1):53–77.
[24] Lee HG, Choi J-W, Kim J. A practically unconditionally gradient stable scheme for the N-component Cahn–Hilliard system. Physica A 2012;391(4):1009–19.
[25] Dong S. An efficient algorithm for incompressible N-phase flows. J Comput Phys 2014;276:691–728.
[26] Dong S. Wall-bounded multiphase flows of N immiscible incompressible fluids: Consistency and contact-angle boundary condition. J Comput Phys 2017;338:21–67.
[27] Yang Z, Dong S. Multiphase flows of N immiscible incompressible fluids: An outflow/open boundary condition and algorithm. J Comput Phys 2018;366:33–70.
[28] Dong S. Multiphase flows of N immiscible incompressible fluids: a reduction-consistent and thermodynamically-consistent formulation and associated algorithm. J Comput Phys 2018;361:1–49.
[29] Liu C, Shen J. A phase field model for the mixture of two incompressible fluids and its approximation by a Fourier-spectral method. Physica D 2003;179(3–4):211–28.
[30] Lowengrub J, Truskinovsky L. Quasi–incompressible Cahn–Hilliard fluids and topological transitions. Proc R Soc Lond Ser A Math Phys Eng Sci 1998;454(1978):2617–54.
[31] Cahn JW, Hilliard JE. Free energy of a nonuniform system. I. Interfacial free energy. J Chem Phys 1958;28(2):258–67.
[32] Shen J. On a new pseudocompressibility method for the incompressible Navier-Stokes equations. Appl Numer Math 1996;21(1):71–90.
[33] Hosseini BS, Turek S, Möller M, Palmes C. Isogeometric analysis of the Navier–Stokes–Cahn–Hilliard equations with application to incompressible two-phase flows. J Comput Phys 2017;348:171–94.

[34] Kopriva DA. Implementing spectral methods for partial differential equations. Springer Netherlands; 2009.

[35] Wheeler MF. An elliptic collocation-finite element method with interior penalties. SIAM J Numer Anal 1978;15(1):152–61.

[36] Ferrer E, Willden RHJ. A high order discontinuous Galerkin finite element solver for the incompressible Navier–Stokes equations. Comput & Fluids 2011;46(1):224–30.

[37] Ferrer E, Willden RHJ. A high order discontinuous Galerkin - Fourier incompressible 3D Navier-Stokes solver with rotating sliding meshes. J Comput Phys 2012;231(21):7037–56.

[38] Ferrer E. An interior penalty stabilised incompressible discontinuous Galerkin - Fourier solver for implicit Large Eddy Simulations. J Comput Phys 2017;348:754–75.

[39] Manzanero J, Rueda-Ramírez AM, Rubio G, Ferrer E. The bassi rebay 1 scheme is a special case of the Symmetric Interior Penalty formulation for discontinuous Galerkin discretisations with Gauss–Lobatto points. J Comput Phys 2018;363:1–10.

[40] Fraysse F, Redondo C, Rubio G, Valero E. Upwind methods for the Baer–Nunziato equations and higher-order reconstruction using artificial viscosity. J Comput Phys 2016;326:805–27.

[41] Redondo C, Fraysse F, Rubio G, Valero E. Artificial viscosity discontinuous Galerkin spectral element method for the Baer-Nunziato Equations. In: Spectral and high order methods for partial differential equations ICOSAHOM 2016. Springer; 2017, p. 613–25.

[42] Gómez-Álvarez S, Rivero-Jiménez A, Rubio G, Manzanero J, Redondo C, et al. Novel coupled Cahn-Hilliard Navier-Stokes solver for the evaluation of oil and gas multiphase flow. In: BHR 19th international conference on multiphase production technology. BHR Group; 2019.

[43] Manzanero J, Rubio G, Kopriva DA, Ferrer E, Valero E. Entropy-stable discontinuous Galerkin approximation with summation-by-parts property for the incompressible Navier-Stokes/Cahn-Hilliard system. J Comput Phys 2020;109363.

[44] Manzanero J, Redondo C, Rubio G, Ferrer E, Valero E, Gómez-Álvarez S, Rivero-Jiménez A. A high-order discontinuous Galerkin solver for multiphase flows. In: Spectral and high order methods for partial differential equations ICOSAHOM 2018. Cham: Springer; 2020, p. 313–23.

[45] Hesthaven JS, Warburton T. Nodal discontinuous galerkin methods: algorithms, analysis, and applications. Springer Science and Business Media; 2007.

[46] Gassner G, Kopriva DA. A comparison of the dispersion and dissipation errors of Gauss and Gauss–Lobatto discontinuous Galerkin spectral element methods. SIAM J Sci Comput 2011;33(5):2560–79.

[47] Moura RC, Sherwin SJ, Peiró J. Linear dispersion–diffusion analysis and its application to under-resolved turbulence simulations using discontinuous Galerkin spectral/hp methods. J Comput Phys 2015;298:695–710.

[48] Manzanero J, Rubio G, Ferrer E, Valero E. Dispersion-dissipation analysis for advection problems with nonconstant coefficients: Applications to discontinuous Galerkin formulations. SIAM J Sci Comput 2018;40(2):A747–68.

[49] Manzanero J, Ferrer E, Rubio G, Valero E. Design of a smagorinsky Spectral Vanishing Viscosity turbulence model for discontinuous Galerkin methods. Comput & Fluids 2020;104440.

[50] Kopriva DA. Metric identities and the discontinuous spectral element method on curvilinear meshes. J Sci Comput 2006;26(3):301.

[51] Kompenhans M, Rubio G, Ferrer E, Valero E. Comparisons of p–adaptation strategies based on truncation– and discretisation–errors for high order discontinuous Galerkin methods. Comput & Fluids 2016;139:36–46, 13th USNCCM, International Symposium of High-Order Methods for Computational Fluid Dynamics - A special issue dedicated to the 60th birthday of Professor David Kopriva.

[52] Kompenhans M, Rubio G, Ferrer E, Valero E. Adaptation strategies for high order discontinuous Galerkin methods based on tau-estimation. J Comput Phys 2016;306:216–36.

[53] Rueda-Ramírez AM, Manzanero J, Ferrer E, Rubio G, Valero E. A p-multigrid strategy with anisotropic p-adaptation based on truncation errors for high-order discontinuous Galerkin methods. J Comput Phys 2019;378:209–33.

[54] G. J. Gassner ARW, Kopriva DA. Split form nodal discontinuous Galerkin schemes with Summation-By-Parts property for the compressible Euler equations. J Comput Phys 2016;327:39–66.

[55] Winters AR, Gassner GJ. Affordable, entropy conserving and entropy stable flux functions for the ideal MHD equations. J Comput Phys 2016;304:72–108.

[56] Manzanero J, Rubio G, Ferrer E, Valero E, Kopriva DA. Insights on aliasing driven instabilities for advection equations with application to Gauss–lobatto discontinuous Galerkin methods. J Sci Comput 2018;75(3):1262–81.

[57] Gassner GJ, Winters AR, Hindenlang FJ, Kopriva DA. The BR1 scheme is stable for the compressible Navier–Stokes equations. J Sci Comput 2018;77(1):154–200.

[58] Manzanero J, Rubio G, Kopriva DA, Ferrer E, Valero E. A free-energy stable nodal discontinuous Galerkin approximation with summation-by-parts property for the Cahn-Hilliard equation. J Comput Phys 2020;403:109072.

[59] Manzanero J, Rubio G, Kopriva DA, Ferrer E, Valero E. An entropy–stable discontinuous Galerkin approximation for the incompressible Navier–Stokes equations with variable density and artificial compressibility. J Comput Phys 2020;408:109241.

[60] Xia Y, Xu Y, Shu C-W. Local discontinuous Galerkin methods for the Cahn–Hilliard type equations. J Comput Phys 2007;227(1):472–91.

[61] Dong S. An efficient algorithm for incompressible N-phase flows. J Comput Phys 2014;276:691–728.

[62] Manzanero J, Redondo C, Rubio G, Ferrer E, Rivero-Jiménez A. A discontinuous Galerkin approximation for a wall–bounded consistent three–component Cahn–Hilliard flow model. Comput & Fluids 2021;225:104971.

[63] Boyer F, Lapuerta C. Study of a three component Cahn-Hilliard flow model. ESAIM Math Model Numer Anal 2006;40(4):653–87.

[64] Williamson JH. Low-storage Runge-Kutta schemes. J Comput Phys.

[65] Redondo C, Chávez-Modena M, Manzanero J, Rubio G, Valero E, Gómez-Álvarez S, Rivero-Jiménez A. CFD–based erosion and corrosion modeling in pipelines using a high–order discontinuous Galerkin multiphase solver. Wear 2021;478–479:203882. http://dx.doi.org/10.1016/j.wear.2021.203882, URL https://www.sciencedirect.com/science/article/pii/S0043164821002714.

[66] Shen J. Pseudo-compressibility methods for the unsteady incompressible Navier-Stokes equations. In: Proceedings of the 1994 beijing symposium on nonlinear evolution equations and infinite dynamical systems; 1997, p. 68–78.

[67] Shen J, Yang X. Energy stable schemes for Cahn-Hilliard phase-field model of two-phase incompressible flows. Chinese Ann Math Ser B 2010;31(5):743–58.

[68] Gassner GJ. A skew-symmetric discontinuous Galerkin spectral element discretization and its relation to SBP-SAT finite difference methods. SIAM J Sci Comput 2013;35(3):1233–56.

[69] Bassi F, Massa F, Botti L, Colombo A. Artificial compressibility Godunov fluxes for variable density incompressible flows. Comput & Fluids 2017;169.

[70] Shahbazi K. Short note: An explicit expression for the penalty parameter of the interior penalty method. J Comput Phys 2005;205(2):401–7.

[71] Shi Y, Wang X-P. Modeling and simulation of dynamics of three-component flows on solid surface. Japan J Ind Appl Math 2014;31(3):611–31.

[72] Xie F, Zheng X, Triantafyllou MS, Constantinides Y, Zheng Y, Karniadakis GE. Direct numerical simulations of two-phase flow in an inclined pipe. J Fluid Mech 2017;825:189–207.

[73] Taitel Y, Dukler A. A model for predicting flow regime transitions in horizontal and near horizontal gas-liquid flow. AIChE J 1976;22(1):47–55.